

Systems survey of endocytosis by multiparametric image analysis

Claudio Collinet¹, Martin Stöter², Charles R. Bradshaw¹, Nikolay Samusik¹, Jochen C. Rink[†], Denise Kenski[†], Bianca Habermann¹, Frank Buchholz¹, Robert Henschel³, Matthias S. Mueller³, Wolfgang E. Nagel³, Eugenio Fava², Yannis Kalaidzidis^{1,4} & Marino Zerial¹

Endocytosis is a complex process fulfilling many cellular and developmental functions. Understanding how it is regulated and integrated with other cellular processes requires a comprehensive analysis of its molecular constituents and general design principles. Here, we developed a new strategy to phenotypically profile the human genome with respect to transferrin (TF) and epidermal growth factor (EGF) endocytosis by combining RNA interference, automated high-resolution confocal microscopy, quantitative multiparametric image analysis and high-performance computing. We identified several novel components of endocytic trafficking, including genes implicated in human diseases. We found that signalling pathways such as Wnt, integrin/cell adhesion, transforming growth factor (TGF)- β and Notch regulate the endocytic system, and identified new genes involved in cargo sorting to a subset of signalling endosomes. A systems analysis by Bayesian networks further showed that the number, size, concentration of cargo and intracellular position of endosomes are not determined randomly but are subject to specific regulation, thus uncovering novel properties of the endocytic system.

Endocytosis is a fundamental process supporting many functions such as nutrient uptake, intracellular signalling¹, morphogenesis during development² and defence against pathogens³. Dysfunctions of the endocytic system lead to severe metabolic⁴, infectious⁵ and neurodegenerative diseases⁶. Receptors are internalized by both Clathrin-dependent and -independent mechanisms into early endosomes and, from here, follow different intracellular routes. For example, transferrin (TF) is recycled back to the plasma membrane, whereas epidermal growth factor (EGF) is routed to late endosomes/lysosomes for degradation. Despite a great deal of molecular insights^{7–9} our understanding of the endocytic machinery remains fragmentary. Furthermore, the design principles of the endocytic pathway, its integration in the overall cellular system and high-order control are still largely unknown. Addressing these problems requires methods capable of seizing the complexity at the system level (that is, measuring many key parameters).

Here, we designed a new analytical approach aimed at phenotypically profiling genes with respect to endocytosis by genome-wide RNAi screening through the quantitative assessment of many system parameters.

Multiparametric profiling of the endocytic system

We visualized endocytosis of fluorescent TF and EGF in HeLa cells before we could apply our platform to more disease-relevant systems. After small interfering RNA (siRNA) transfection, cells internalized the two cargo markers simultaneously for 10 min, were fixed, stained with 4',6-diamidino-2-phenylindole (DAPI)/SYTO42 blue for nuclei and cytoplasm detection, and imaged (12 images per well) by triple-colour high-resolution automated confocal microscopy (Fig. 1a).

Instead of performing a phenotypic evaluation on the basis of single or few parameters as commonly done in previous screens^{10,11}, we developed a quantitative multiparametric image analysis (QMPIA)

platform, on the basis of the custom-designed image analysis software MotionTracking¹². First, images were segmented to determine morphological and positional descriptors for each endosome (Fig. 1b). Second, a total set of 62 parameters were extracted, 4 serving as quality control to reject sub-optimal images and 58 describing defined biological properties of the endocytic system, such as total internal cargo, number, size (mean apparent area) and position of endosomes (Fig. 1c, Supplementary Table 1 and Supplementary Information for details). The latter were processed to suppress plate-to-plate random variations, normalized (see Supplementary Information) and the 46 most robust parameters (see Supplementary Information and Supplementary Table 1) were combined into multiparametric profiles (Fig. 1d) describing quantitatively the endocytic phenotypes.

In preparation for the genomic screen, we validated the quality and reproducibility of assay and QMPIA. First, we verified that the depletion of established components of the endocytic machinery, such as Clathrin (CLTC), Dynamin-2 (DNM2), EGF receptor (EGFR), Transferrin receptor (TFRC), early endosome antigen 1 (EEA1) and others by RNAi (Supplementary Figs 1 and 2), yielded the expected alterations in phenotypic profiles. For example, silencing of *TFRC* reduced the values of number of endosomes, total internal cargo and mean cargo load per endosome for TF but not EGF (Fig. 1d and Supplementary Fig. 1e). Conversely, *EGFR* downregulation perturbed the parameters of EGF but not of TF (Supplementary Fig. 1e). Second, we validated the use of a single confocal section as representative of the three-dimensional endosomal population of the entire cell (Supplementary Fig. 3). Third, we validated the reproducibility of the observed phenotypic profiles using the same and different siRNAs targeting the same gene for a set of 78 genes and 468 siRNA (6 siRNAs per gene). We found that profiles of the same siRNAs were highly reproducible (Fig. 2a) (mean Pearson correlation coefficient 0.6 ± 0.02 s.e.m.), compared with other monoparametric screens¹³

¹Max Planck Institute for Molecular Cell Biology and Genetics, ²High-Throughput Technology Development Studio, MPI-CBG, Pfotenhauerstrasse 108, 01307 Dresden, Germany. ³Center for Information Services and High Performance Computing (ZIH), Dresden University of Technology, D-01062 Dresden, Germany. ⁴Belozersky Institute of Physico-Chemical Biology, Moscow State University, 119899, Moscow, Russia. [†]Present addresses: University of Utah School of Medicine, 401 MREB, 20 North 1900 East, Salt Lake City, Utah 84132-3401, USA (J.C.R.); Sirna Therapeutics Inc., San Francisco, California 94158, USA (D.K.).

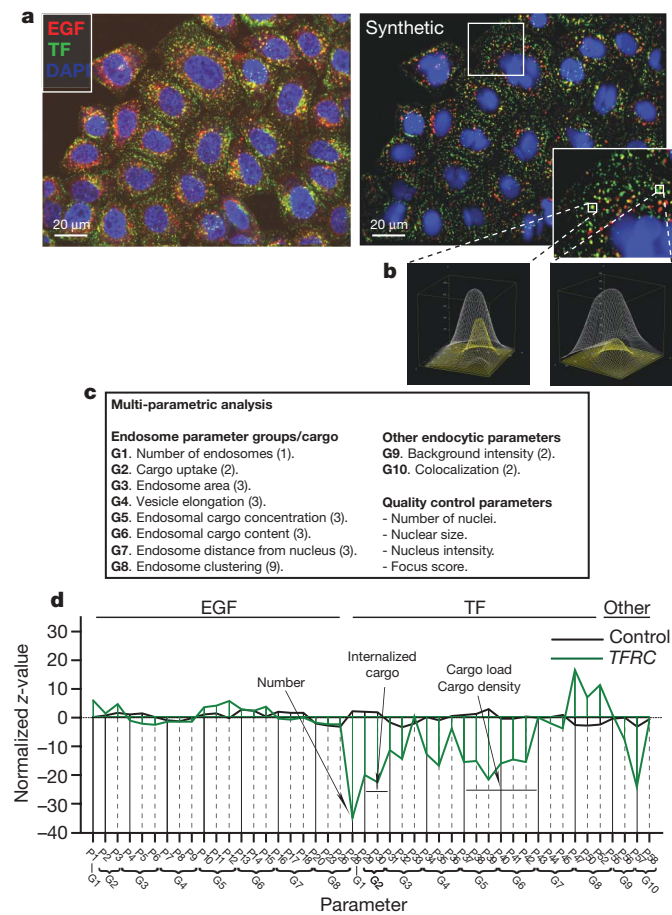


Figure 1 | Multiparametric image analysis. **a**, Example of three-colour high-resolution images collected with the automated spinning disk confocal OPERA microscope (left). Nuclei and cytoplasm are pseudo-coloured in blue, Alexa-488-labelled EGF is pseudo-coloured in red and Alexa-647-labelled TF is pseudo-coloured in green. The synthetic image (right) was obtained after background intensity subtraction and modelling of endosomal structures (see Supplementary Information). **b**, Close-ups show the model structure of individual endosomes. **c**, List of quantitative parameters divided into groups (G1–G10). Ten groups of parameters (number of parameters in each group indicated in brackets) were used to measure endosomal features and four parameters as image quality control. See Supplementary Table 1 and Supplementary Information for further description on the QMPIA parameters. **d**, Example of QMPIA profile (TFRC; see pictures in Supplementary Fig. 1c). The 46 most specific parameters (listed in Supplementary Table 1 and Supplementary Information) are aligned on the x-axis and normalized z-values are plotted on the y-axis. Parameter groups (G1–G10) and parameter numbers (P1–P58) are indicated corresponding to the nomenclature in **c** and to the enumeration in Supplementary Table 1, respectively. Black continuous lines separate the parameter groups and grey dashed lines separate the parameters. The horizontal bars indicate the endocytic markers which the parameters refer to. Key parameters affected in the TFRC profile are indicated by arrows.

(see Supplementary Information), indicating that the experimental noise is not increased by the higher complexity of the assay. In contrast, different siRNAs targeting the same gene frequently yielded different profiles (Fig. 2b) (mean Pearson correlation coefficient 0.047 ± 0.01 s.e.m.), consistent with high incidence of RNAi off-target^{13–17}. As we excluded variations in protein depletion and silencing of alternatively spliced transcripts (data not shown), the major cause of incoherence between profiles of different siRNAs is most probably off-target effects.

Gene phenotypic profiling

Assuming that each siRNA profile has both ‘on-target’ and ‘off-target’ phenotypic components, we exploited the QMPIA to suppress as much as possible the latter contaminant. For this, we developed a

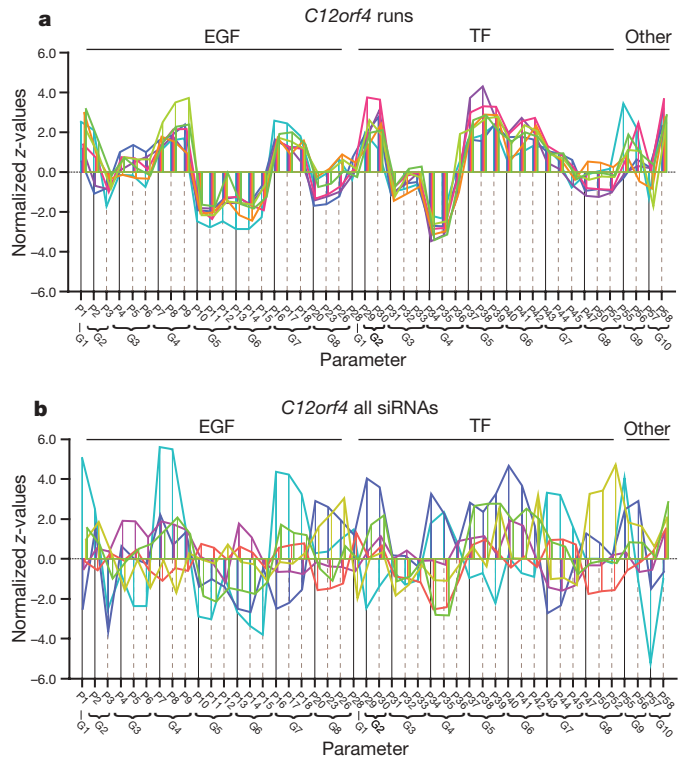


Figure 2 | Reproducibility of multiparametric profiles by the same siRNA and different siRNAs/gene. **a**, Reproducibility of multiparametric profiles of a single siRNA silencing the *C12orf4* gene. The same siRNA (ID: 28470) was transfected in seven independent experiments (runs) and multiparametric profiles (differently coloured for each experiment) were calculated and plotted as described in Fig. 1. **b**, Reproducibility of multiparametric profiles of different siRNAs targeting the same gene (*C12orf4*). *C12orf4* was silenced with six different siRNAs (IDs: 133085, 133086, 133087, 28285, 28378, 28470) in the same experiment and corresponding multiparametric profiles were calculated and plotted as described in Fig. 1.

probabilistic approach to infer gene-specific phenotypes by ‘averaging’ the profiles of different siRNAs targeting the same gene. We defined the ‘gene profile’ as the most probable profile calculated as mode of the a posteriori joint probability distribution considering all individual siRNA profiles for a given gene. Notably, here every siRNA targeting a given gene contributes, to a different extent, to the determination of gene profiles (see Supplementary Fig. 4), circumventing the need of similarity thresholds to define supporting siRNAs (2 of 3, 3 of 3, and so on)¹⁸. Gene profiles instead of individual siRNA profiles were subsequently used for phenotypic clustering and gene classification.

As test, we screened 1,000 genes including 35 known endocytic regulators (Supplementary Table 2) and 92 kinases identified in a previous screen¹⁹ (Supplementary Table 3) using seven siRNAs per gene. On the basis of the QMPIA, 31 of the 35 endocytic regulator genes (~90%) and 62 out of 92 kinase genes presented a χ^2 probability $(1.0 - P) \geq 0.95$ corresponding to a statistically significant enrichment ($P = 1.1 \times 10^{-11}$ and $P = 5 \times 10^{-12}$, respectively) in the list of scores. Interestingly, only 7 out of the 35 endocytic regulators would have scored considering only two parameters (EGF and TF total internal cargo). Altogether, these data indicate that the QMPIA has the advantage of higher comprehensiveness and specificity over monoparametric read-outs in the identification of genes regulating endocytic trafficking.

Genome-wide survey of EGF and TF endocytosis

To improve accuracy and coverage in the survey, we screened directly in the primary assay three genomic libraries, two siRNA and one endoribonuclease-prepared siRNA (esiRNA)¹⁵, corresponding to

7–8 si/esRNAs per gene for a total of 161,492 si/esRNAs (see Methods). This approach presents two major advantages. First, the high number of si/esRNAs analysed by QMPIA reduces the impact of false negatives owing to disagreement between siRNAs. Second, reproducibility of phenotypes is assessed already in the primary screen for all genes (not just the hits). We acquired 12 images per sample to obtain statistically significant data, accounting for a total of $\sim 2.5 \times 10^6$ images. Quality controls for transfection efficiency, QMPIA and toxicity (see Methods) were included in each plate (see Supplementary Fig. 5). Image analysis and gene profile determination required $\sim 4.5 \times 10^6$ CPU hours of calculation on a 2,584-cores computer cluster.

Phenotypic clustering and gene scoring

As our aim was not to identify a few hit genes but rather to conduct a systems analysis, we exploited the multidimensionality of gene profiles. First, we clustered all genes of the human genome using mean-shift clustering²⁰ (see Supplementary Information). We identified 14 phenotypic cluster groups (Fig. 3) stable over a wide range of the algorithm parameters, indicating that the endocytic system is under constraints and changes between a discrete set of possible states in response to perturbations. Second, genes were scored on the basis of two criteria, phenotype amplitude (probability of χ^2) and presence of specific phenotypic traits (defined as the cluster group profiles; ‘pheno-score’; Supplementary Information), as shown in Supplementary Fig. 6,

providing both strong and mild, but specific, phenotypes. A list of 4,609 genes, 3,804 with a ‘strong’ and 805 with a ‘mild’ phenotype was compiled (Supplementary Table 4; images and profiles available at <http://gwsdisplayer.mpi-cbg.de>). Considering both the design of the assay and the integration of endocytosis with many cellular processes, such a large number was expected because, besides the ‘core’ endocytic machinery, many genes have a direct or indirect role in endocytosis. For comparison with the common practices in the field, we estimated that screening a single library (2–3 siRNAs per gene) with a typical two-parameter assay and validating the hits with an independent set of si/esRNAs (4–5) would yield only 336 genes (data not shown), indicating that the large number of genes in the list results from (1) a broader window of detection (many parameters) and (2) high number of si/esRNAs screened rather than permissive criteria for selection.

To estimate the reproducibility of the hits, we re-screened twice the kinome-phosphatome (9,330 siRNAs, 1,459 genes), including a large fraction of the gene hits (235). We observed 84% reproducibility for ‘strong’ and 72.5% for ‘mild’ phenotypes. Nevertheless, to assign a better probabilistic value to the scores, the genes in the list will be re-screened (the web database will be updated). The silencing efficacy of the libraries was assessed by the manufacturers by quantitative RT–PCR (qRT–PCR) on a set of siRNAs and we independently confirmed it by western blotting (see Methods and Supplementary Fig. 7).

The largest portion of scored genes ($\sim 34\%$, 1,593; P -value of enrichment $P = 7 \times 10^{-34}$) encoded for components of metabolic

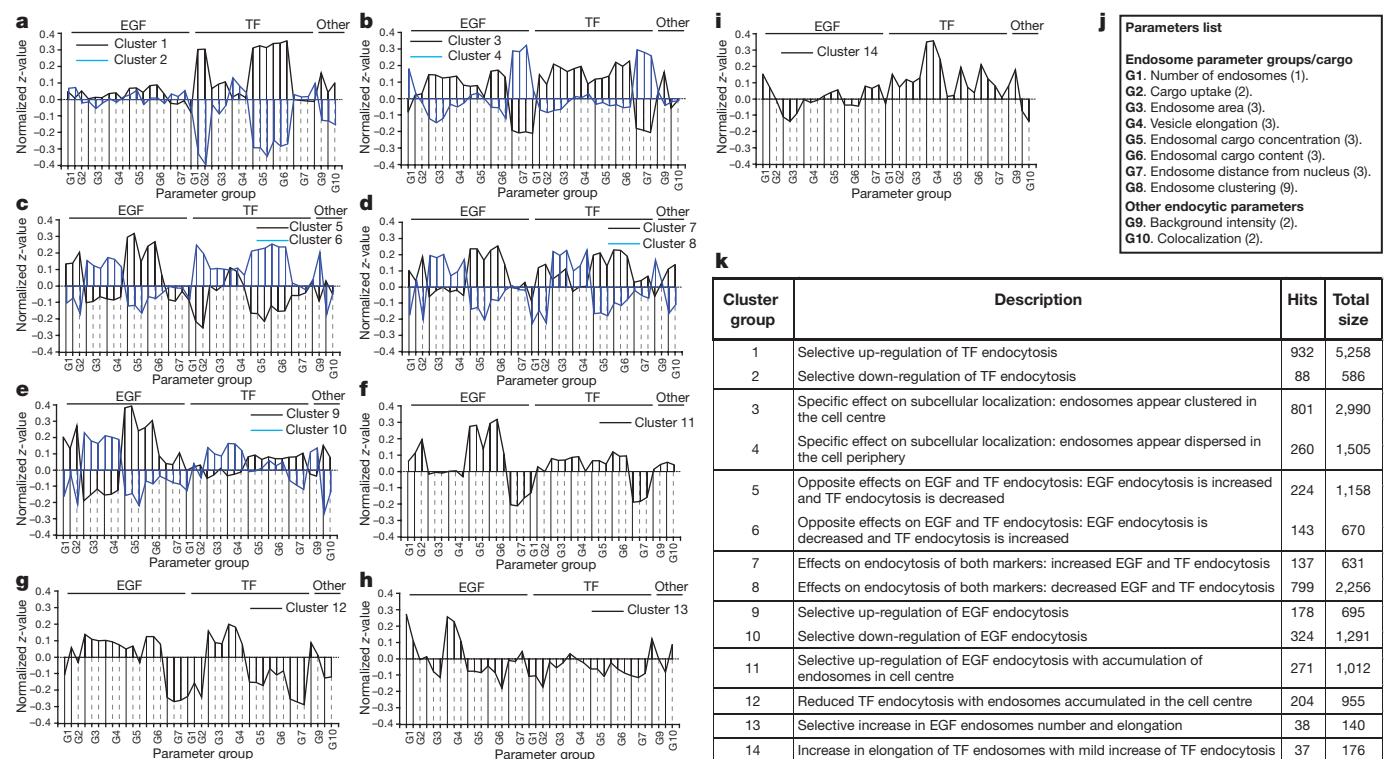


Figure 3 | Phenotypic cluster groups profiles. **a–i**, Mean-shift genomic clustering of the gene profiles (see text and Supplementary Information) yielded 14 cluster groups. Multiparametric profiles of the cluster groups are plotted as in Fig. 1. The amplitude of the phenotype vectors was normalized to 1. **a**, Cluster group 1 (black) and cluster group 2 (blue) present selective and opposite effects, that is, increased vs decreased internal TF, respectively. **b**, Cluster group 3 (black) and cluster group 4 (blue) present specific and opposite effects on the subcellular localization of endosomes (‘distance from nucleus’); that is, endosomes are either clustered in the perinuclear region (cluster group 3) or dispersed in the periphery (cluster group 4). **c**, Cluster group 5 (black) and cluster group 6 (blue) is a pair of opposite clusters presenting each opposite effects with respect to EGF and TF endocytosis: increased EGF endocytosis with concomitantly decreased TF endocytosis (cluster group 5) and vice-versa (cluster group 6). **d**, Cluster group 7 (black)

and cluster group 8 (blue) present opposite effects on endocytosis of both EGF and TF (both increased for cluster group 7, both decreased for cluster group 8). **e**, Cluster group 9 (black) and cluster group 10 (blue) present selective and opposite effects on EGF endocytosis: increased and decreased, respectively. **f**, Cluster group 11 presents increased EGF endocytosis and endosome accumulation in the perinuclear region. **g**, Cluster group 12 presents reduced TF endocytosis and endosomes accumulated in the cell centre. **h**, Cluster group 13 presents a selective increase in EGF endosomes number and their elongation. **i**, Cluster group 14 presents mainly an increase in TF endosomes elongation. **j**, List of parameter-groups compiled as in Fig. 1c. **k**, Table providing a summary of the most representative phenotypes in each group (‘Description’). The number of hits and the total size of each group are also indicated.

and signalling pathways; 10% (468, $P = 1 \times 10^{-214}$) could bioinformatically be assigned to the 'core' endocytic machinery, embracing established (*CLTC*, *DNM2*, *EEA1*) and predicted genes on the basis of trafficking-relevant functional domains, such as VPS9 (8/10; $P = 6 \times 10^{-4}$), TBC (13/38; $P = 0.18$), FYVE-finger (9/27; $P = 0.27$)²¹, PX (14/41; $P = 0.17$) or BAR (4/15; $P = 0.59$)²² domains. Some genes (17%; 798; $P = 1 \times 10^{-36}$) were 'unknown' owing to absence of curated annotations. We found several novel potential endocytic regulators such as four TBC domain-containing proteins (MGC16169 (also known as *TBCK*), *TBC1D9*, *TBC1D9B*, *TBC1D21*), two FYVE-finger proteins (*MTMR4* and *WDFY1*), and a protein with a VPS9 domain (*RINL*). Notably, the list was enriched in genes implicated in different human diseases (Kyoto Encyclopedia of Genes and Genomes database; see Supplementary Information) such as different cancers (for example, glioma ($P = 1.26 \times 10^{-8}$), colorectal ($P = 5.53 \times 10^{-6}$), pancreatic cancer ($P = 8.92 \times 10^{-6}$) etc.), neurodegenerative and metabolic disorders (for example, dentatorubral-pallidolusian atrophy; $P = 7.8 \times 10^{-3}$), Huntington disease ($P = 0.026$) and type II diabetes ($P = 3.7 \times 10^{-3}$).

Regulation by metabolic and signalling pathways

The cluster analysis provided insights into how endocytosis is integrated with other cellular functions and made predictions concerning the function of uncharacterized genes. Many cluster groups were anti-correlated (Fig. 3a–e and Supplementary Fig. 8a, b), reflecting positive and negative regulation on the endocytic system. For example, ablation of genes in cluster groups 1 and 2 increased and decreased the amount of internalized TF, respectively (Fig. 3a and Supplementary Fig. 8a). Interestingly, genes of metabolic pathways were highly enriched in cluster group 1, most probably reflecting a compensatory response to a metabolic deficit by generally increasing endocytosis of nutrients.

Another example of anti-correlated phenotypes is provided by cluster groups 3 and 4 (Fig. 3b and Supplementary Fig. 8b), where the endosomes were localized either closer to or more distant from the nuclei, respectively. We found enrichment ($P = 0.022$ in cluster group 3 and $P = 2.3 \times 10^{-3}$ in cluster group 4) of components of the actin and tubulin cytoskeleton (for example, *RAC1*, *ROCK2*, *CAPZB*, microtubule and actin motors *KIF20A* and *MYH9*). Interestingly, in cluster group 4 we found genes involved in cytokinesis such as *CEP55* (ref. 23) and *KIF20A* (ref. 24), strengthening the link with endocytosis²⁵.

Cluster groups 8 and 10 contained several known endocytic components. Cluster group 8 (decreased internal TF and EGF; Fig. 3d) contained many genes encoding components required for endocytic uptake, such as *CLTC*, *DNM2* and phosphatidylinositol kinases/phosphatases (*INPP4A*, *INPP5B*, *PIB5PA*, *INPPL1*; $P = 1.48 \times 10^{-7}$). Cluster group 10 contained several endosomal regulators such as Rabankyrin-5 (*ANKFY1*)²⁶, Rabenosyn-5 (*ZFYVE20*)²⁷ and Hrs (*HGS*), indicating that EGF endocytosis is particularly susceptible to depletion of PI(3)P effectors. On the basis of these results, we predict that many new components of the endocytic core machinery are in these cluster groups.

Signalling pathways exert distinct effects on the endocytic system. Here we confirmed the activity of mitogen-activated protein kinase (MAPK), Ca^{2+} , integrin/cell adhesion and mTOR signalling pathways^{19,28} and uncovered the activity of several new ones, TGF- β /activin, Wnt and Notch. Some (MAPK, Ca^{2+} , mTOR, Wnt) had a wide range of effects on the endocytic system (enriched in several cluster groups; not shown) but others produced very specific effects (enriched in single or opposite groups). For example, in cluster groups 3 and 4 we found enrichment in the integrin/cell adhesion pathway ($P = 0.012$ in cluster group 3 and $P = 6.6 \times 10^{-4}$ in cluster group 4; *ITGA5*, *ITGB1*, *ITGA9*, *PAK1*, *MAPK9*, *MAPK1*).

Interestingly, the Notch and TGF- β pathways were enriched ($P = 0.026$ and $P = 5.6 \times 10^{-3}$, respectively) in cluster group 8 (reduced total internal cargo for both EGF and TF). As we excluded

the possibility that the reduction in total internal cargo was due to downregulation of surface receptors (Supplementary Fig. 9), we suggest a new role of these pathways in the regulation of endocytic uptake. We found for the Notch pathway *NOTCH4*, *PSENEN* and *PSEN2*, *MAML1* and *RBPJ* and for the TGF- β pathway several genes encoding for activin receptors (*ACVR1B*, *ACVR2A*, *ACVR2B* and *ACVRL1*).

In conclusion, the cluster analysis assigns new functions to metabolic and signalling pathways and further predicts functions for new genes in endocytosis.

Differential regulation of TF and EGF trafficking

To reveal general design principles of the endocytic system we considered all ~160,000 knockdown conditions as independent perturbed states of the system and determined correlations between parameters. A first interesting aspect emerging from such analysis was a high divergence in EGF and TF endocytosis. Despite the good correlation between the size of EGF- and TF-positive endosomes (Fig. 4a) and their intracellular localization (Fig. 4b), we found an unexpected low correlation between the levels of total internal cargo (Fig. 4c) of the two markers. These results strongly indicate that although the molecular regulators of endosome size and distance from nucleus are essentially shared by EGF and TF, the machineries controlling internalization and sorting are largely distinct. We exclude a major contribution of alternative non-clathrin-dependent entry pathways²⁹ under our experimental conditions, because depletion of *CLTC* almost completely blocked the uptake of both cargo markers (Supplementary Fig. 1a). One possible interpretation is that EGF and TF may preferentially be internalized into endocytic vesicles subjected to different regulation. For example, depletion of AP-2 complex specifically reduces TF but not EGF internalization (Supplementary Fig. 10)³⁰, whereas knockdown of other genes such as *PLEKHB2*, *CCDC33* and *RCHY1* specifically downregulated EGF internalization.

Interestingly, silencing of certain genes resulted in the dispersal of EGF into small, peripheral endosomes (Fig. 4e), a pattern reminiscent of APPL1-endosomes³¹. These endosomes are largely distinct from canonical EEA1-positive early endosomes³¹ and act as signalling platforms³². Knockdown of *ZFYVE20*, *ANKFY1*, *PIK3R1*, *PIK3R2* along with novel genes such as *CCDC128* (also known as *KLRAQ1*), *C12orf4*, *MGC16169* (also known as *TBCK*) specifically affected EEA1-positive endosomes (Fig. 4d–e) and increased the colocalization of EGF with APPL1 (Fig. 4h–i). Conversely, knockdown of *INPP5B* and *RABEP1* specifically affected APPL1-positive endosomes (Fig. 4d–f) and concomitantly decreased their colocalization with EGF (Fig. 4h–i). Altogether, we identified new components that regulate the sorting of EGF to APPL1-positive endosomes.

New design principles of the endocytic system

Our analysis also showed that various endosomal parameters are significantly correlated and, therefore, functionally linked. For both EGF (Fig. 5a–c) and TF, we observed a negative correlation between mean size and number of endosomes, a positive correlation between the number of endosomes and their mean distance from nucleus and a negative correlation between endosome size and distance from nucleus. Total internal cargo and cargo concentration per endosome (Fig. 5d) as well as number of endosomes (Fig. 5e) were also strongly correlated positively. In contrast, there was no correlation between total internal cargo and endosome size (Fig. 5f) and their distance from nucleus (not shown).

The analysis of pair correlations indicate that the endocytic parameters are functionally linked, but does not infer cause–effect relationships. To infer directionality in these relationships and learn general rules underlying the organization of the endocytic system, we performed a Bayesian network analysis. The structure of Bayesian networks is a directed acyclic graph where nodes denote the variables of interest and edges correspond to logical dependencies between

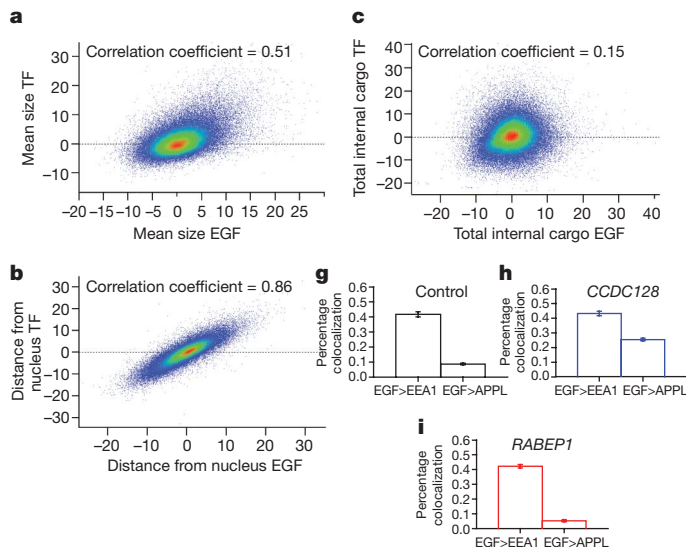
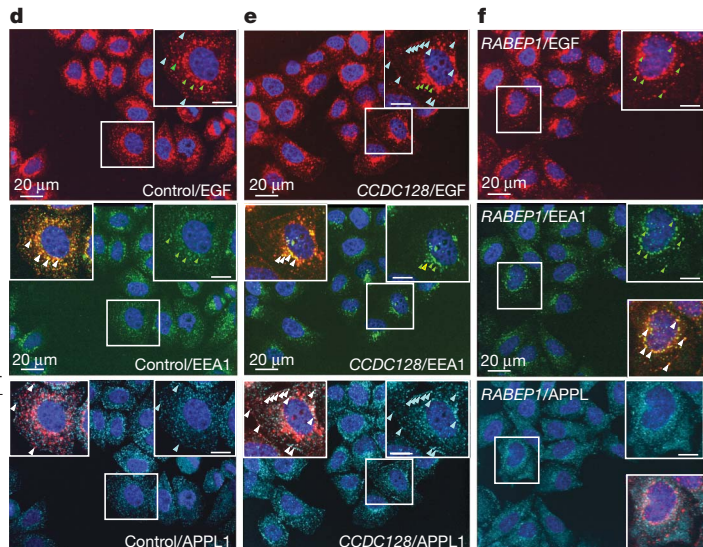


Figure 4 | Regulators of transport of cargo to EEA1 vs APPL endosomes. **a–c**, Correlation between endosome size (**a**), endosome distance from nuclei (**b**) and total internal cargo (**c**) for both EGF and TF. The data are represented as scatter plots of z-score values. The density of the data point is indicated in blue for low- and in red for high-density values. Pearson correlation values (correlation coefficient) are indicated for each scatter plot. **d–f**, Examples of knockdown of genes affecting the accumulation of EGF in APPL1-positive endosomes. HeLa cells silenced for the indicated genes were fixed and stained for the indicated markers. **d**, Mock-transfected control cells. **e**, Silencing of *CCDC128* selectively affected EEA1 endosomes (enlarged endosomes in the perinuclear region), determining the accumulation of EGF in APPL1-positive endosomes. **f**, Silencing of *RABEP1*



reduced the endosomal staining of APPL1 determining an increase of the cytoplasmic staining. Insets show higher magnifications to visualize better the endosomal (co)-localization. Merge insets show always EGF overlaid on the indicated endosomal marker. Scale bars, 10 μm. White arrows indicate the presence of EGF in the APPL1 and EEA1-positive endosomes in the EGF and EEA1 insets. Green arrows indicate the presence of EEA1 on the indicated endosomes in the EGF and EEA1 insets. Light blue arrows indicate the presence of APPL1 on the indicated endosomes in the EGF and APPL1 insets. **g–i**, Quantification of EGF colocalization with the markers indicated. EGF-to-APPL colocalization is increased upon silencing of *CCDC128* (**h**) and decreased upon silencing of *RABEP1* (**i**) compared to control cells (**g**). Error bars indicate standard error of the mean (s.e.m.).

them³³. We constructed two Bayesian networks for EGF and TF (Fig. 5g–h), where the nodes correspond to the ‘key’ phenotypic parameters and the edges to their pair correlation. The two networks shared a similar structure. Surprisingly, for both EGF and TF the parameter measuring endosome distance from nucleus was found to influence other parameters, indicating a key regulatory role in

the endocytic system. The dependencies between the triplet endosome distance from nucleus–number–size reflect a progression from many small peripheral to few large perinuclear endosomes. Genes involved in protein ubiquitination were found enriched among the regulators of this process (cluster group 4 $P = 0.032$). We found *RBX1* and *DDBI*, encoding components of a multiprotein complex

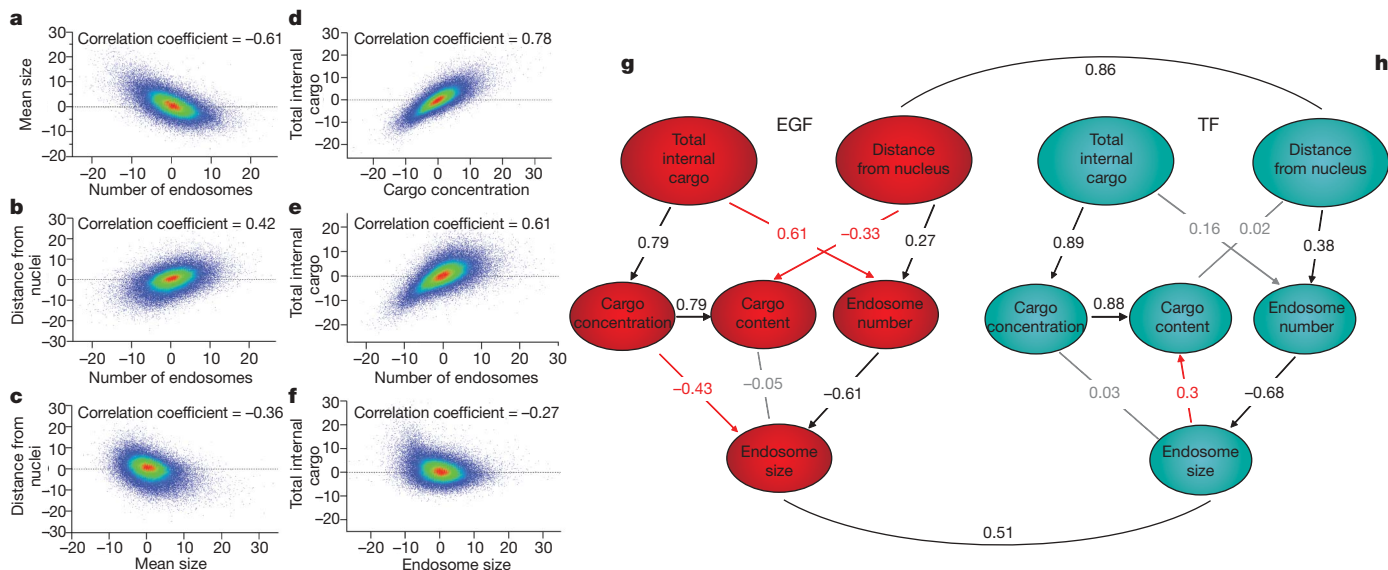


Figure 5 | Design principles of the endocytic system. **a–f**, Analysis of correlations between different endocytic parameters. The data are represented as in Fig. 4 and only correlations between EGF parameters are shown: negative correlation between endosome size and number (**a**), positive correlation between number and distance from nuclei (**b**), negative correlation between endosome size and endosomes distance from nuclei (**c**), positive correlation between total internal cargo and mean endosome concentration (**d**), positive correlation between total internal cargo and

endosome number (**e**) and weak correlation between total internal cargo and endosome size (**f**). **g–h**, Bayesian networks of the endocytic parameters for the genome-wide analysis of EGF and TF endocytosis. The nodes represent individual endocytic parameters measuring EGF or TF endocytosis and the numbers indicate the Pearson correlation values. In black the direct correlations shared by the two networks, in red (present) and grey (absent) correlations that present differences between the two networks.

including cullins catalysing ubiquitin ligation³⁴ and other genes such as *FBXO22*, *FBXO30*, *FBXO46*, *FBXO6*, *USP31* and *HECTD3*, indicating a new role of protein ubiquitination in the endosomal spatio-temporal progression.

However, the two networks also presented some interesting differences. The negative dependency of endosome cargo content on distance from nucleus reflects a progressive concentration of EGF in endosomes, in contrast to TF that is continuously removed and recycled to the surface. A comparison of the triplet concentration–size–content revealed some unexpected properties of the endocytic system. The TF network has a structure typical of passively sorted membrane proteins, where cargo content depends on size and concentration of cargo per endosome. In contrast, the mean concentration of EGF in the endosomes is adjusted so that the mean total content of EGF per endosome remains constant, independently of endosome size (negative dependence of the size on the concentration and no correlation between size and content). Such a mechanism cannot be explained only by sorting of EGF into intra-luminal vesicles⁹, because (1) this is inconsistent with the high correlation between size of EGF and TF endosomes and (2) the knockdown of *HGS* (Hrs) and *TSG101* (ref. 9) does not alter the size–concentration–content relationship. These data rather indicate the existence of a quasi-deterministic mechanism tightly coupling fusion and fission events to regulate the concentration of EGF in each endosome.

Finally, the cell exerts a tighter control on the number of EGF- than TF-positive endosomes, as indicated by the stronger dependence on total internal cargo ($corr_{EGF} = 0.61$ vs $corr_{TF} = 0.16$). In other words, to increase cargo capacity the system in addition to concentrating EGF in endosomes (as for TF) also generates new endosomes.

Altogether, these findings indicate that the cell regulates the number, size, loading and, therefore, the intracellular density of EGF-bearing endosomes. These findings have profound implications for the role of endosomes in signalling^{31,35,36}.

Discussion

As a first step towards a systems analysis of endocytosis, we profiled the human genome relative to a set of 58 parameters that quantitatively describe endocytic features. From this survey we could attribute new functions to known and unknown (798) genes with respect to EGF and TF endocytosis. Furthermore, we revealed unexpected properties of the endocytic system. First, we uncovered the effect of various signalling pathways, notably integrin/cell adhesion, TGF- β , Notch and Wnt, on both TF and EGF endocytosis. The activity of these pathways depends on endocytosis^{37–39}, but our data further indicate that they exert a feedback mechanism on the endocytic machinery. Interestingly, TGF- β , Notch and Wnt pathways have been implicated in the regulation of epithelial–mesenchymal transition (EMT)⁴⁰, cell-fate determination⁴¹ and tissue morphogenesis⁴² and given the established role of endocytosis in these events^{2,43}, we propose that part of their morphogenetic activity depends on their effects on the endocytic pathway. Second, a surprising result was the low correlation between genes regulating TF and EGF endocytosis (Figs 5g–h and 4a–c). Differences in the molecular machinery regulating cargo uptake and recycling have been reported³⁰, but such a degree of diversity is unprecedented. Third, our analysis provided insights into the design principles underlying the endocytic system. The fact that the endosome distance from the nucleus is a key regulatory parameter demonstrates directly that the spatio-temporal progression of endosomes observed in living cells¹² is not an epiphenomenon but has a fundamental role in the function of the endocytic system. The many components of the actin and tubulin cytoskeleton identified in the screen (cluster groups 3 and 4) provide insights into the molecular regulation underlying this mechanism.

An interesting aspect emerging from the comparison of the EGF and TF Bayesian networks is that the cell specifically regulates the number of EGF-positive endosomes, and strictly couples size and concentration of cargo in endosomes. Given that endosomes can

act as intracellular signalling platforms^{32,35}, the system might regulate the concentration of EGF and the number of EGF-positive endosomes to quantitatively control signalling responses, for example, for different cell-fate decisions, as shown for the MAPK network⁴⁴. Regulating the density of receptor tyrosine kinases, and number and distribution of endosomes may be necessary to calibrate the concentration of signalling molecules and their signalling output. In identifying genes that selectively affect cargo transport to APPL1-positive endosomes, we unveiled a sorting mechanism to distribute cargo to this compartment. This is the beginning of a more detailed molecular characterization of APPL1 endosomes, their regulation of transport and their role in signal propagation^{32,35}. However, a limitation of our approach remains the poor identification of highly homologous and functionally redundant genes (for example, *RAB5A*, *B*, *C* and so on). This could be overcome by combinations of several siRNAs, as for *CBL*, *CBLB* and *CBLC* (Supplementary Table 4).

This exploratory endeavour required uncommon resources for a primary screen. Nevertheless, it was necessary to establish the conditions for streamlining the technology and rendering such genomic profiling easier and more affordable in the future. Several genes identified in the screen are associated with human diseases, confirming the fundamental role of endocytosis in the pathogenesis of many human diseases and providing novel potential drug targets. It will be important to determine which parameters of the QMPIA might act as physiopathological indicators reflecting disease-relevant alterations. When applied to primary cells and disease model systems, the screening platform described here will reveal its true potential for drug discovery, through the identification of novel therapeutic targets, new mechanisms of action, and for discerning therapeutic effects of small molecules from toxic ones.

METHODS SUMMARY

RNAi screen for endocytosis. HeLa cells were reverse transfected with three genomic libraries (Ambion, Qiagen and a custom-made esiRNA library¹⁵) using 20 nM siRNAs or 25 ng per well esiRNAs. Seventy-two hours after transfection, cells were incubated with 100 ng ml⁻¹ EGF-Alexa 488 and 5 μ g ml⁻¹ Transferrin-Alexa 647 (Molecular Probes) in serum-free medium for 10 min at 37 °C before fixation with formaldehyde. Thereafter, nuclei and cytoplasm were stained with 0.4 μ g ml⁻¹ DAPI and 0.2 μ M SYTO42 blue (Molecular Probes).

Automated image acquisition. Triple-colour images were acquired in a fully automated and unbiased manner using a spinning disk confocal microscope (OPERA, Evotec Technologies-PerkinElmer) and a $\times 40$ water immersion objective (NA = 0.9). Twelve images per well were collected to obtain a sufficient number of cells for reliable statistical analysis. Image correction and image analysis were performed using custom designed image analysis software (MotionTracking; see Supplementary Information).

EAA1-APPL1 endosome dissection of EGF trafficking. Genes of interest (78) were screened to detect alterations in the EEA1- or APPL1-positive endosomes with respect to EGF trafficking. Following siRNA transfection and EGF-Alexa 488 internalization, cells were stained with mouse monoclonal anti-EAA1 (BD Biosciences; Pharmingen) and rabbit polyclonal anti-APPL1 (ref. 31) antibodies and quadruple-colour images were acquired as described (Methods).

Detection of surface receptors. To exclude changes in the level of surface receptors upon downregulation of Notch and TGF- β signalling pathways, cells were transfected with si/esiRNAs targeting these genes and 1,034 randomly selected si/esiRNAs, incubated with 100 ng ml⁻¹ EGF-Alexa 488 and 5 μ g ml⁻¹ TF-Alexa 647 (Molecular Probes) in serum-free medium for 30 min on ice, fixed and stained with DAPI-SYTO42 as described earlier. Signals were enhanced by staining with a rabbit anti-Alexa 488 (Molecular Probes) and mouse monoclonal antibodies against the ectodomain of human TFRC (BD Biosciences; Pharmingen) without permeabilization. Triple-colour images (ten per well) were collected with a $\times 20$ water immersion objective (NA = 0.7) as described earlier.

Full Methods and any associated references are available in the online version of the paper at www.nature.com/nature.

Received 1 December 2008; accepted 17 December 2009.

Published online 28 February; corrected 11 March 2010 (see full-text HTML version for details).

1. Polo, S. & Di Fiore, P. P. Endocytosis conducts the cell signaling orchestra. *Cell* **124**, 897–900 (2006).

2. Dudu, V., Pantazis, P. & González-Gaitán, M. Membrane traffic during embryonic development: epithelial formation, cell fate decisions and differentiation. *Curr. Opin. Cell Biol.* **16**, 407–414 (2004).
3. Burgdorf, S. & Kurts, C. Endocytosis mechanisms and the cell biology of antigen presentation. *Curr. Opin. Immunol.* **20**, 89–95 (2008).
4. Pagano, R. E., Puri, V., Dominguez, M. & Marks, D. L. Membrane traffic in sphingolipid storage diseases. *Traffic* **1**, 807–815 (2000).
5. Gruenberg, J. & van der Goot, F. G. Mechanisms of pathogen entry through the endosomal compartments. *Nature Rev. Mol. Cell Biol.* **7**, 495–504 (2006).
6. Baskys, A., Bayazitov, I., Zhu, E., Fang, L. & Wang, R. Rab-mediated endocytosis: linking neurodegeneration, neuroprotection, and synaptic plasticity? *Ann. NY Acad. Sci.* **1122**, 313–329 (2007).
7. Marsh, M. & McMahon, H. T. The structural era of endocytosis. *Science* **285**, 215–220 (1999).
8. Stenmark, H. Rab GTPases as coordinators of vesicle traffic. *Nature Rev. Mol. Cell Biol.* **10**, 513–525 (2009).
9. Piper, R. C. & Katzmann, D. J. Biogenesis and function of multivesicular bodies. *Annu. Rev. Cell Dev. Biol.* **23**, 519–547 (2007).
10. Perrimon, N. & Mathey-Prevot, B. Applications of high-throughput RNA interference screens to problems in cell and developmental biology. *Genetics* **175**, 7–16 (2007).
11. Friedman, A. & Perrimon, N. A functional RNAi screen for regulators of receptor tyrosine kinase and ERK signalling. *Nature* **444**, 230–234 (2006).
12. Rink, J., Ghigo, E., Kalaidzidis, Y. & Zerial, M. Rab conversion as a mechanism of progression from early to late endosomes. *Cell* **122**, 735–749 (2005).
13. König, R. *et al.* A probability-based approach for the analysis of large-scale RNAi screens. *Nature Methods* **4**, 847–849 (2007).
14. Kulkarni, M. M. *et al.* Evidence of off-target effects associated with long dsRNAs in *Drosophila melanogaster* cell-based assays. *Nature Methods* **3**, 833–838 (2006).
15. Kittler, R. *et al.* Genome-wide resources of endoribonuclease-prepared short interfering RNAs for specific loss-of-function studies. *Nature Methods* **4**, 337–344 (2007).
16. Birmingham, A. *et al.* 3' UTR seed matches, but not overall identity, are associated with RNAi off-targets. *Nature Methods* **3**, 199–204 (2006).
17. Cullen, B. R. Enhancing and confirming the specificity of RNAi experiments. *Nature Methods* **3**, 677–681 (2006).
18. Echeverri, C. J. *et al.* Minimizing the risk of reporting false positives in large-scale RNAi screens. *Nature Methods* **3**, 777–779 (2006).
19. Pelkmans, L. *et al.* Genome-wide analysis of human kinases in clathrin- and caveolae/raft-mediated endocytosis. *Nature* **436**, 78–86 (2005).
20. Fukunaga, K. & Hostetler, L. The estimation of the gradient of a density function, with applications in pattern recognition. *IEEE Trans. Inf. Theory* **21**, 32–40 (1975).
21. Hayakawa, A., Hayes, S., Leonard, D., Lambright, D. & Corvera, S. Evolutionarily conserved structural and functional roles of the FYVE domain. *Biochem. Soc. Symp.* **74**, 95–105 (2007).
22. Habermann, B. The BAR-domain family of proteins: a case of bending and binding? *EMBO Rep.* **5**, 250–255 (2004).
23. Carlton, J. G. & Martin-Serrano, J. Parallels between cytokinesis and retroviral budding: a role for the ESCRT machinery. *Science* **316**, 1908–1912 (2007).
24. Hill, E., Clarke, M. & Barr, F. A. The Rab6-binding kinesin, Rab6-KIFL, is required for cytokinesis. *EMBO J.* **19**, 5711–5719 (2000).
25. Baluska, F., Menzel, D. & Barlow, P. W. Cytokinesis in plant and animal cells: endosomes 'shut the door'. *Dev. Biol.* **294**, 1–10 (2006).
26. Schnatwinkel, C. *et al.* The Rab5 effector Rabankyrin-5 regulates and coordinates different endocytic mechanisms. *PLoS Biol.* **2**, e261 (2004).
27. Nielsen, E. *et al.* Rabenosyn-5, a novel Rab5 effector, is complexed with hVPS45 and recruited to endosomes through a FYVE finger domain. *J. Cell Biol.* **151**, 601–612 (2000).
28. Galvez, T. *et al.* siRNA screen of the human signaling proteome identifies the PtdIns(3,4,5)P3-mTOR signaling pathway as a primary regulator of transferrin uptake. *Genome Biol.* **8**, R142 (2007).
29. Sigismund, S. *et al.* Clathrin-independent endocytosis of ubiquitinated cargos. *Proc. Natl Acad. Sci. USA* **102**, 2760–2765 (2005).
30. Motley, A., Bright, N. A., Seaman, M. N. & Robinson, M. S. Clathrin-mediated endocytosis in AP-2-depleted cells. *J. Cell Biol.* **162**, 909–918 (2003).
31. Miaczynska, M. *et al.* APPL proteins link Rab5 to nuclear signal transduction via an endosomal compartment. *Cell* **116**, 445–456 (2004).
32. Schenck, A. *et al.* The endosomal protein Appl1 mediates Akt substrate specificity and cell survival in vertebrate development. *Cell* **133**, 486–497 (2008).
33. Pearl, J. *Probabilistic Reasoning in Intelligent Systems: Networks of Plausible Inference* (Morgan Kaufmann, 1988).
34. Petroski, M. D. & Deshaies, R. J. Function and regulation of cullin-RING ubiquitin ligases. *Nature Rev. Mol. Cell Biol.* **6**, 9–20 (2005).
35. Miaczynska, M., Pelkmans, L. & Zerial, M. Not just a sink: endosomes in control of signal transduction. *Curr. Opin. Cell Biol.* **16**, 400–406 (2004).
36. Kermorgant, S. & Parker, P. J. Receptor trafficking controls weak signal delivery: a strategy used by c-Met for STAT3 nuclear accumulation. *J. Cell Biol.* **182**, 855–863 (2008).
37. Huang, S. S. & Huang, J. S. TGF- β control of cell proliferation. *J. Cell. Biochem.* **96**, 447–462 (2005).
38. Le Borgne, R. Regulation of Notch signalling by endocytosis and endosomal sorting. *Curr. Opin. Cell Biol.* **18**, 213–222 (2006).
39. Gagliardi, M., Piddini, E. & Vincent, J. P. Endocytosis: a positive or a negative influence on Wnt signalling? *Traffic* **9**, 1–9 (2008).
40. Heldin, C. H., Landström, M. & Moustakas, A. Mechanism of TGF- β signaling to growth arrest, apoptosis, and epithelial-mesenchymal transition. *Curr. Opin. Cell Biol.* **21**, 166–176 (2009).
41. Blank, U., Karlsson, G. & Karlsson, S. Signaling pathways governing stem-cell fate. *Blood* **111**, 492–503 (2008).
42. Weinmaster, G. Notch signal transduction: a real rip and more. *Curr. Opin. Genet. Dev.* **10**, 363–369 (2000).
43. Entchev, E. V. & González-Gaitán, M. A. Morphogen gradient formation and vesicular trafficking. *Traffic* **3**, 98–109 (2002).
44. Santos, S. D., Verveer, P. J. & Bastiaens, P. I. Growth factor-induced MAPK network topology shapes Erk response determining PC-12 cell fate. *Nature Cell Biol.* **9**, 324–330 (2007).

Supplementary Information is linked to the online version of the paper at www.nature.com/nature.

Acknowledgements We acknowledge T. Galvez and G. Marsico, members of the Zerial group for discussions and scientific support. We are particularly indebted to K. Korn who developed transfection protocols and organized various preparatory steps and logistics before the screen and E. Krausz for the management of the HT-TDS, the MPI-CBG screening facility. We thank J. Schmitt, A. Lohmann, S. Christ, N. Tomschke, A. Niederlein, J. Wagner, M. Gierth, E. Krausz for technical, robotics and computational assistance, and M. Boes and J. Oegema for IT support that made the large-scale computational analysis possible. We acknowledge I. C. Baines, T. Galvez, J. Howard, T. Hyman, M. McShane, G. O'Sullivan and P. Tomancak for comments on the manuscript. This work was financially supported by the Max Planck Society (MPG) and by the systems biology network HepatoSys of the German Ministry for Education and Research BMBF, the DFG and the Gottlieb Daimler und Karl Benz Stiftung. This work is also part of the project 'Endotrack', which received research funding from the European Community's Sixth Framework Programme.

Author Contributions C.C., Y.K. and M.Z. conceived the project and M.Z. directed it. C.C. and D.K. developed the endocytosis assay under the guidance of M.Z. and E.F.; M.S. performed the screen and image acquisition. Y.K. developed the QMPIA with the help of C.C. and J.C.R. and performed all computational analysis of the screening data. N.S. developed the clustering and pheno-score algorithms and together with C.C. performed the analysis of the clusters. C.R.B., under the supervision of B.H., performed the si/esiRNAs remapping and bioinformatics analysis. CC. and Y.K. performed the Bayesian Network analysis. F.B. provided the esiRNA library. R.H., under the supervision of M.S.M. and W.E.N., provided IT support for the use of the computer cluster located at the TUD. C.C., Y.K. and M.Z. wrote the manuscript.

Author Information Reprints and permissions information is available at www.nature.com/reprints. The authors declare no competing financial interests. Correspondence and requests for materials should be addressed to M.Z. (zerial@mpi-cbg.de).

METHODS

siRNA and esiRNA libraries and remapping to RefSeq 28. Three genomic RNAi libraries, two commercial siRNA libraries (Ambion Silencer Genome wide siRNA Library V.3 and Qiagen Human Whole Genome siRNA Library V.1) and a custom-made esiRNA library¹⁵ were screened. The Ambion library included 51,880 siRNAs targeting 22,527 genes in the human genome and was designed partly on the basis of the RefSeq database Release 15 and partly on the ENSEMBL database. The Qiagen library, which included 91,956 siRNAs targeting 22,732 genes, was entirely designed on the basis of the RefSeq database (kinase/phosphatase and gpcr subsets: Refseq Release 18, Druggable Genome Set: Refseq Release 17, the rest of the Whole Genome Set and the Predicted Genes Set RefSeq Release 12). The esiRNA library was prepared as described previously¹³ and included 17,188 esiRNAs targeting 16,722 human genes, designed on the basis of the ENSEMBL (Release 36) database. Ambion and Qiagen validated 768 and 3,073 siRNAs by qRT-PCR, respectively. Out of these, 740 (Ambion) and 3,072 (Qiagen) were shown to be efficient (>70% reduction) at silencing their corresponding target mRNAs, providing an overall estimated efficiency of >95% for the Ambion and >99% for the Qiagen libraries, respectively. The sequences of all 3 libraries were remapped on the RefSeq Release 28 database by BLAST. The sequence of an siRNA or esiRNA was mapped to a given gene on the basis of the following three conditions: (1) 19/19 bases match on a region on the mRNA, (2) matching with all transcripts (including differentially spliced mRNAs) of a given gene, (3) absence of matching with any other transcripts from other genes. All siRNAs/esRNAs that did not meet these conditions were discarded from further analysis. After re-mapping to RefSeq Release 28, the 3 libraries covered 33,223 genes of which 28,279 encode for proteins or contain an open reading frame, corresponding to 62% coverage of the transcriptome and 73% of the proteome.

HT RNAi transfection and endocytic assay. HeLa cells were reverse transfected with 20 nM siRNAs or 25 ng per well esiRNAs (final concentration) with 0.2 μ l per well Oligofectamine (Invitrogen) in a total volume of 50 μ l. For HT-transfection a 'Freedom Evo' pipetting robot (Tecan) equipped with a 384-fixed-needle-head, an 8-needle-pipettor and a gripper was used under a customized biological safety cabinet. A fully automated workflow prepared transfection complexes in 384 wells at a throughput of 5 plates/50 min (manuscript submitted). For cell seeding and dispensing the assay solutions the MTP dispensers WellMate and Multidrop 384 (Thermo Scientific) were used; wash procedures were performed using the Power Washer 384 (Tecan).

Briefly, 10 μ l of 200 nM siRNAs or 5 ng μ l⁻¹ esiRNAs were mixed with 10 μ l of pre-diluted Oligofectamine (40 μ l ml⁻¹ OptiMem) for 15 min to allow complex formation. Subsequently, 10 μ l of this mixture were placed in 384-well CellCarrier plates (Evotec Technologies). HeLa cells (1000 cells per well, counted with CASY Model TT, Schärfe System) were seeded in 40 μ l per well. Plates were

incubated for 72 h at 37 °C and 5% CO₂. Thereafter, the cells were incubated with 100 ng ml⁻¹ EGF-Alexa 488 and 5 μ g ml⁻¹ transferrin-Alexa 647 (Molecular Probes) in serum-free medium for 10 min at 37 °C. Cells were subsequently washed with PBS and fixed with 3.7% formaldehyde. Nuclei and cytoplasm were stained with 0.4 μ g ml⁻¹ DAPI and 0.2 μ M SYTO42 blue (Molecular Probes). For the analysis of protein downregulation, cells were grown in 96-well plates and transfected with 20 nM siRNAs (final concentration) with 0.3 μ l per well Oligofectamine (Invitrogen) in a total volume of 100 μ l. After 72 h total protein extracts were prepared and analysed by quantitative western blotting using antibodies against EEA1, ZFYVE20 and ANKFY1.

Automated spinning disk confocal imaging. Twelve images per well were collected with a \times 40 water immersion objective (NA = 0.9) in a fully automated and unbiased manner with a spinning disk confocal microscope (OPERA, Evotec Technologies-Perkin Elmer). Triple-colour images were acquired in two sequential exposures by three different CCD cameras: the Alexa 488 signal was collected in a first exposure using 488 nm laser light and a 540/75 band-pass filter; Alexa 647 and DAPI-SYTO 42 blue signals were collected in a second exposure using 635 nm and 405 nm laser light and with 700/90 and 450/50 band-pass filters, respectively. Images were subsequently corrected (MotionTracking; see Supplementary Information) for uneven field illumination and chromatic aberrations according to reference images. For reference, images of 2.5 μ m multicolour beads, and images of reference dyes and dark field images were collected using the Opera Adjustment Plate (Evotec Technologies-Perkin Elmer).

Three-dimensional imaging of the endosome distribution of the cell was performed on a small set of 27 siRNAs (targeting 10 genes of the human genome). Using the same microscope and automated imaging protocols as above 10 focal planes with 0.5 μ m steps were acquired.

EEA1-APPL1 endosome dissection of EGF trafficking. A smaller set of 78 genes was further screened to detect alterations in the EEA1- or APPL1-positive endosomes with respect to EGF trafficking. For this, cells were transfected, EGF-Alexa 488 was internalized and cells were fixed as above. Cells were then permeabilized with 0.1% saponin and 0.2% fish gelatin (as blocking agent) and subsequently stained with mouse monoclonal anti-EEA1 (BD Biosciences Pharmingen) and rabbit polyclonal anti-APPL1 (ref. 31) antibodies. Fluorescently conjugated goat anti-rabbit-Alexa 568 and goat anti-mouse-Alexa 647 secondary antibodies (Molecular Probes) revealed the antigen signals and DAPI-SYTO 42 blue stained the nuclei and cytoplasm. Quadruple-colour confocal images were collected (OPERA, Evotec Technologies-PerkinElmer) in two sequential exposures: Alexa 488 and Alexa 647 signals were collected in a first exposure using 488 nm and 635 nm laser light and with 540/75 and 690/50 band pass filters; Alexa 568 and DAPI-SYTO 42 blue signals were collected in a second exposure using 405 nm and 561 nm laser light and with 450/50 and 605/40 band-pass filters, respectively. Reference images were acquired and image correction performed as before.